Linking particle properties to dense suspension extrusion flow characteristics using discrete element simulations

Christopher Ness,[1,2] Michele Marigo,[3] Paul McGuire,[3]

Han Xu,[3] Hugh Stitt,[3] Jin Y. Ooi,[1] and Jin Sun[1]

[1]*School of Engineering, University of Edinburgh,*

Edinburgh EH9 3JL, United Kingdom

[2]*Department of Chemical Engineering and Biotechnology,*

University of Cambridge, Cambridge CB3 0AS, United Kingdom

[3]*Johnson Matthey Technology Centre, Billingham,*

PO Box 1, TS23 1LB, United Kingdom

(Dated: March 6, 2017)

Abstract

Extrusion is a widely used process for forming suspensions and pastes into designed shapes, and is central to the manufacture of many products. In this article, the extrusion through a square-entry die of non-Brownian spheres suspended in Newtonian fluid is investigated using discrete element simulations, capturing individual particle-particle contacts and hydrodynamic interactions. The simulations reveal inhomogeneous velocity and stress distributions, originating in the inherent microstructure formed by the constituent particles. Such features are shown to be relevant to *generic* paste extrusion behaviour, such as extrudate swell. The pressure drop across the extruder is correlated with the extrudate flow rate, with the empirical fitting parameters being linked directly to particle properties such as surface friction, and processing conditions such as extruder wall roughness. Our model and results bring recent advances in suspension rheology into an industrial setting, laying foundations for future model development, predictive paste formulation and extrusion design.

LIST OF FIGURES

1 Schematic of the extrusion geometry showing barrel, die entry and die as represented by different particle shadings, with flow direction from left to right as indicated. Dashed arrows indicate the dimensions in units of particle diameters d; solid arrows indicate the coordinate definition. The geometry is $5d$ deep in the z-direction, with a periodic boundary condition on front and back. The dashed box at the far left illustrates the particle insertion and force application region. 36

2 Close-up image of die entry region, to illustrate the bounding walls composed of nonmoving, smaller particles. 37

3 Velocity profile in the extruder for simulation Case A with $\Delta P = 5 \times 10^5$Pa. (a) Velocity contour plot showing the total velocity magnitude V scaled by the mean centreline downstream velocity in the barrel V^{barrel}. Annotations show the locations of four pressure transducers; (b) Streamlines associated with (a); Velocity profiles along (c) $y = 0$, showing the locations of the barrel and die; (d) $x = 150$; (e) $x = 400$. 39

4 Velocity gradients at the die entry for simulation Case A with $\Delta P = 5\times10^5$Pa, showing shear gradients (a) dV_x/dy; (b) dV_y/dx and extensional gradients (c) dV_x/dx; (d) dV_y/dy. Velocity gradients are scaled with $\rho d^2/\eta_f$ such that the color scale represents Stokes numbers with respect to each flow gradient: (a) St_{xy}; (b) St_{yx}; (c) St_{xx} and (d) St_{yy}. Stokes numbers remain $\ll 1$ in all regions. 40

5 Time-averaged static zone size for simulation Case A, counting all particles within the static zones, as a function of the die velocity V^{die}. 41

6 Internal stress profiles for simulation Case A with $\Delta P = 5 \times 10^5$Pa. (a) Pressure P, scaled by the mean pressure at the upstream end ($25 < x < 50$) of the barrel, P^{barrel}; (b) Shear stress σ_{xy}, scaled by P^{barrel}; (c) First normal stress difference $N_1 = \sigma_{xx} - \sigma_{yy}$, scaled by P^{barrel}; (d) First normal stress difference N_1, scaled by the mean pressure at the upstream end ($300 < x < 325$) of the die, P^{die}. 42

7 Rate of energy dissipation per unit volume for simulation Case A, calculated as $S = \boldsymbol{\sigma} : \dot{\boldsymbol{\gamma}}$, where S has units of $\rho d^2/t^3$. 43

8 Stress ratio and volume fraction in the barrel and die. (a) Stress ratio σ_{xy}/P profile in the barrel for Cases A-F; (b) Stress ratio σ_{xy}/P profile in the die for Cases A-F; (c) Volume fraction profile across the barrel for Case A; (d) Volume fraction profile across the die for Case A. 44

9 Pressure drops are wall stresses versus die velocity for simulation Cases A - F, as described in Table I, with the pressures measured at the locations highlighted in Figure 3. (a) Total pressure drop across extruder ($P_1 - P_4$); (b) Barrel pressure drop ($P_1 - P_2$); (c) Die-entry pressure drop ($P_2 - P_3$); (d) Die pressure drop ($P_3 - P_4$). Dashed black line in each figure indicates a gradient of unity; (e) Wall stresses in barrel; (f) Wall stress in die. 45

INTRODUCTION

Highly concentrated dispersions of solid particles in a liquid, such as suspensions and pastes, are found throughout industry. Extrusion is a ubiquitous process for forming such pastes into complex predetermined shapes, and is a crucial step in the manufacture of many consumer and chemical products, such as porcelains and catalyst supports[1]. To meet increasing technical demands on finished product structure and performance, improvements to existing manufacturing methods are urgently required. Even minor changes to formulation or operating conditions can, however, result in flow instabilities and product defects that are very challenging to predict with the models currently available[2–5].

During extrusion, the paste is forced to flow through a constriction with inlet/outlet cross-sectional area ratio A_0/A, and along a narrow die of length L and perimeter M, giving a product of desired composition and dimensions. The classical expression used to relate the pressure drop ΔP required to achieve an extrudate velocity V is given by Benbow and Bridgwater[1] as

$$\Delta P = (\sigma_0 + \alpha V^m) \ln\left(\frac{A_0}{A}\right) + (\tau_0 + \beta V^n)\frac{ML}{A}, \tag{1}$$

where the first term on the right hand side represents the die-entry pressure drop, and the second term is the wall friction contribution. α, β, m, n, σ_0, τ_0 are related to the bulk constitutive material properties and processing conditions, and can be calibrated using experimental data[6]. This semi-empirical expression has become popular for both industrial

and academic extrusion pressure calculations[7]. It relies on a continuum description of the material rheology, and assumes the paste can be characterised simply by a bulk yield stress σ_0 and a zero-velocity wall shear stress τ_0 in addition to power-law shear-rate dependence[8].

In reality, the pastes being extruded are disordered, amorphous, solid-liquid assemblies[9] whose rheology typically exhibits many non-linearities such as yield stress behaviour[10], shear thinning[11] and shear thickening[12–15], as well as time-dependence[16] and non-locality[17]. These phenomena derive at the particle level and are governed by details of the particle-scale physics as demonstrated recently for the case of shear thickening in a series of experimental and numerical works (see, for example[18–20]), and traditional continuum rheological models, for example Bingham or Herschel-Bulkley, cannot provide a *comprehensive* description of the rheology across flow regimes[21]. Moreover, in extreme cases the flow confinement may be such that separation of scales between the die geometry A and a typical particle diameter d is only one order of magnitude or less, rendering the dynamics more comparable to, for example, discharging grains[22,23], than to those of a continuous non-Newtonian fluid. In such scenarios, the discrete nature of the paste is of paramount importance to the rheology and continuum models break down. A further complicating flow phenomenon of particular interest is liquid phase migration (LPM)[24,25], the net movement of liquid down an internal pressure gradient. LPM results in localised fluctuations in the solids content of the paste, leading to regions of increased viscosity[26,27] or undesired plastic or quasi-static behaviour in an otherwise viscous flow[28–30], rendering a continuum description of the material highly challenging. Several studies of ram extrusion have found strong evidence that the onset of LPM, proven to be present both by post-extrusion drying, weighing and analysis of extrudate samples, and by ram force-time profiles, is correlated with ram velocity[25,31–33]. It is more likely to occur at low velocities[25,33], where the convection of liquid through a slower moving solid matrix is more prevalent. Furthermore, it has been proposed that in addition to localised pressure gradients, LPM during extrusion can also be caused by suction effects due to the extensional strain rate imposed on the paste at the die entry[31,32,34].

As a result of these complications, Equation 1 may, if suitably calibrated, offer a practical determination of the energy input required for specific extrusion processes, but it does not have predictive capability for new materials whose constitutive behaviour is unknown, or not describable simply as Herschel-Bulkley or Bingham. It is clear, therefore, that new constitutive equations relating particle properties and particle-scale structural and stress

information to processing parameters[35,36] are required to provide thorough and predictive alternative models for extrusion, in order to meet the future challenges in paste formulation and process design.

A number of semi-empirical constitutive models have been proposed to address this issue specifically for extrusion flow in industrial and consumer materials[37,38], using experimentally observed flow features to build upon the traditional constitutive equations[39]. Such models typically correlate temporal microstructural changes during extrusion to bulk rheological properties. For example, Engmann and Mackley[40] modelled chocolate during cold extrusion as a Bingham plastic by dynamically relating the yield stress to the energy required to convert the constituent crystalline particles to a liquid state. Similarly, the Carreau Model, a constitutive equation typically used for describing the rheology of polymers, has been adapted[41] to describe the microstructural evolution of PTFE paste during extrusion. This allows the model to begin to predict shear-thickening behaviour as the microstructure develops during extrusion, giving remarkable agreement with experimental data.

In the present work, we address this need for a stronger rational link between particle-scale physics and process-level extrusion rheology. Discrete element method (DEM) simulations are carried out, resolving the velocities and contacts of all suspended particles using an interaction model that has been demonstrated to successfully capture the shear rheology of suspensions[42,43] with convincing experimental agreement. We investigate pressure-driven extrusion flow through a square-entry die, and present the resulting internal velocity and stress profiles predicted by the model. These profiles provide a general description of extrusion flow governed at the particle-, rather than bulk-, scale, and may serve as a template for future constitutive descriptions of paste rheology. We further elucidate the links between the observed bulk extrusion behaviour and the particle-scale properties by assessing whether the flow may be described according to the Benbow-Bridgwater equation, and explicitly considering the relationships between particle stiffness, particle friction, liquid viscosity and wall roughness and the α and β Benbow-Bridgwater parameters. Overall, our results highlight the discrete nature of the paste and allow us to shed light on the links between microscale physics and macroscale extrusion phenomena, providing a foundational basis for the development of future constitutive equations as well as guiding future practice for industrial paste formulation and process design. Our model and the present results are relevant to processing of soft matter in general, and may have broad impact and utility across industry.

DESCRIPTION OF SIMULATION MODEL

Contact model for particle and hydrodynamic interactions

We consider a model dense suspension or paste composed of purely repulsive spherical particles, density (ρ) matched with an interstitial Newtonian liquid of constant viscosity η_f. The paste is bidisperse, being composed of a 1:1 mixture, by number, of particles with diameters d and $1.5d$. Such a particle size distribution is adopted to prevent crystallisation as occurs for monodisperse particles[44,45]. We verified that no segregation of particle sizes occurs spatially or temporally at any point during the simulation. The paste is non-Brownian, meaning particle thermal diffusion is negligible when compared to advection under the driving flow. This non-Brownian limit, corresponding to Péclet number Pé ($= 3\pi\eta_f\dot{\gamma}d^3/4kT$) $\gg 1$ for characteristic advection rate $\dot{\gamma}$ and thermal energy kT, arises in dense suspensions of both silica and polymethylmethacrylate, for example, under typical processing conditions[20]. The equation of motion for the suspended particles can be written simply as[46]

$$m\frac{d}{dt}\begin{pmatrix}\mathbf{v}\\ \boldsymbol{\omega}\end{pmatrix} = \sum\begin{pmatrix}\mathbf{F}\\ \boldsymbol{\Gamma}\end{pmatrix}, \tag{2}$$

for particles of mass m with translational and rotational velocity vectors $\mathbf{v}$ and $\boldsymbol{\omega}$ respectively, subjected to force and torque vectors $\mathbf{F}$ and $\boldsymbol{\Gamma}$ respectively. For the model paste studied in this work, forces and torques arising due to direct contacts between neighbouring particles ($\mathbf{F}^c, \boldsymbol{\Gamma}^c$) and through particle-fluid hydrodynamic interactions ($\mathbf{F}^h, \boldsymbol{\Gamma}^h$) are considered. Full solution of the hydrodynamic forces has previously been achieved computationally using the Stokesian Dynamics algorithm[47–49], which resolves long-range, many-body interactions in addition to short-range pairwise, divergent lubrication films. The great computational expense of such an approach makes large simulations (> 3000 particles) challenging. For very dense suspensions, for which the mean neighbouring-particle separation becomes extremely small relative to the particle diameter, the divergent lubrication resistances dominate the hydrodynamic interaction[50], while long-range hydrodynamic interactions are screened by the presence of numerous intervening particles. $\mathbf{F}^h$ and $\boldsymbol{\Gamma}^h$ can therefore be approximated by summing pairwise lubrication forces among neighbouring particles ([42,50–53] and others). For an interaction between particles i and j, the hydrodynamic force and torque on particle

i can be expressed as

$$\begin{aligned}\mathbf{F}_{ij}^{h} &= -a_{sq}6\pi\eta_f(\mathbf{v}_i-\mathbf{v}_j)\cdot\mathbf{n}_{ij}\mathbf{n}_{ij} \\ &\quad - a_{sh}6\pi\eta_f(\mathbf{v}_i-\mathbf{v}_j)\cdot(\mathbf{I}-\mathbf{n}_{ij}\mathbf{n}_{ij}),\end{aligned} \tag{3a}$$

$$\begin{aligned}\mathbf{\Gamma}_{ij}^{h} &= -a_{pu}\pi\eta_f d_i^3(\boldsymbol{\omega}_i-\boldsymbol{\omega}_j)\cdot(\mathbf{I}-\mathbf{n}_{ij}\mathbf{n}_{ij}) \\ &\quad - \frac{d_i}{2}\left(\mathbf{n}_{ij}\times\mathbf{F}_i^l\right).\end{aligned} \tag{3b}$$

for particle diameter d_i, centre-to-centre unit vector from j to i $\mathbf{n}_{ij}$ and identity tensor $\mathbf{I}$. The squeeze a_{sq}, shear a_{sh} and pump a_{pu} resistance terms, derived by[54] for $\beta = d_j/d_i$, are given by

$$\begin{aligned}a_{sq} &= \frac{\beta^2}{(1+\beta)^2}\frac{d_i^2}{4h_{\text{eff}}} + \frac{1+7\beta+\beta^2}{5(1+\beta)^3}\frac{d_i}{2}\ln\left(\frac{d_i}{2h_{\text{eff}}}\right) \\ &\quad + \frac{1+18\beta-29\beta^2+18\beta^3+\beta^4}{21(1+\beta)^4}\frac{d_i^2}{4h_{\text{eff}}}\ln\left(\frac{d_i}{2h_{\text{eff}}}\right),\end{aligned} \tag{4a}$$

$$\begin{aligned}a_{sh} &= 4\beta\frac{2+\beta+2\beta^2}{15(1+\beta)^3}\frac{d_i}{2}\ln\left(\frac{d_i}{2h_{\text{eff}}}\right) \\ &\quad + 4\frac{16-45\beta+58\beta^2-45\beta^3+16\beta^4}{375(1+\beta)^4}\frac{d_i^2}{4h_{\text{eff}}}\ln\left(\frac{d_i}{2h_{\text{eff}}}\right),\end{aligned} \tag{4b}$$

$$\begin{aligned}a_{pu} &= \beta\frac{4+\beta}{10(1+\beta)^2}\ln\left(\frac{d_i}{2h_{\text{eff}}}\right) \\ &\quad + \frac{32-33\beta+83\beta^2+43\beta^3}{250(1+\beta)^3}\frac{d_i}{2h_{\text{eff}}}\ln\left(\frac{d_i}{2h_{\text{eff}}}\right).\end{aligned} \tag{4c}$$

For each pairwise interaction, the interparticle gap, i.e. the surface-to-surface distance h, is calculated according to $h = |\mathbf{r}_{ij}| - \frac{d_i+d_j}{2}$ for centre-to-centre vector $\mathbf{r}_{ij}$. These lubrication forces are inherently dissipative. The forces are proportional to the relative velocities of neighbouring particles so that particle motions will tend to be rapidly dampened whenever the lubrication force is calculated. An increasing body of experimental work[11,19] indicates that direct particle-particle surface contacts can play a major role in determining paste viscosity; indeed, simulations that strictly resolve hydrodynamic forces, treating particles as ideally hard and ideally smooth[55], have proven to be inadequate for capturing dense suspension rheology for cases where particle-particle contacts are presumed to be important. Moreover, even simulations that capture the elasto-hydrodynamic deformation of particles under large lubrication forces[56] have proven insufficient to capture the large viscosities of suspended frictional particles. We therefore truncate the lubrication divergence and regularize the contact singularity at a typical asperity length scale $h_{\min} = 0.001d_{ij}$ for weighted

average particle diameter $d_{ij} = \frac{d_i d_j}{d_i + d_j}$, i.e., setting $h = h_{\min}$ in the force calculation, when $h < h_{\min}$, allowing particles to come into contact. The effective interparticle gap used in the force calculation, h_{eff}, is therefore given by

$$h_{\text{eff}} = \begin{cases} h & \text{for } h > h_{\min} \\ h_{\min} & \text{otherwise.} \end{cases} \tag{5}$$

For computational efficiency, the lubrication forces are omitted when the interparticle gap h is greater than $h_{\max} = 0.05 d_{ij}$. The volume fraction is sufficiently high that all particles have numerous neighbours within this range, so such an omission is inconsequential to the dynamics, as we verified elsewhere[42]. When a lubrication film between two particle surfaces ruptures (this occurs when $h < 0$), the particle interaction is defined according to a purely repulsive linear spring model[57], with normal $\mathbf{F}^{c,n}$ and tangential $\mathbf{F}^{c,t}$ forces and torque $\mathbf{\Gamma}^c$ given by

$$\mathbf{F}^{c,n}_{ij} = k_{\text{n}} \delta \mathbf{n}_{\text{ij}}, \tag{6a}$$

$$\mathbf{F}^{c,t}_{ij} = -k_{\text{t}} \mathbf{u}_{\text{ij}}, \tag{6b}$$

$$\mathbf{\Gamma}^c_i = -\frac{d_i}{2}(\mathbf{n}_{ij} \times \mathbf{F}^{c,t}_{i,j}), \tag{6c}$$

for a collision between particles i and j with normal and tangential spring stiffnesses k_n and k_t respectively, particle overlap δ and tangential displacement $\mathbf{u}_{\text{ij}}$, updated incrementally during each contact. We note that the damping arising from hydrodynamic interactions is always sufficient to achieve a steady state, so further damping in the particle-particle contact model, a typical feature of simulations of dry granular matter[58], is omitted for simplicity. A particle-particle Coulomb friction coefficient μ_p is defined according to $|\mathbf{F}^{c,t}_{i,j}| \leq \mu_p |\mathbf{F}^{c,n}_{i,j}|$, setting a maximal value for the tangential force exerted during a collision. This friction coefficient sets a critical force value for which contacting particles will slide past each other rather than roll over each other. In addition, a particle-wall friction coefficient μ_w is defined, regulating the maximal tangential force that may be exerted by the wall on any particle. The particle diameter d sets a characteristic length scale for the simulation, while the stiffness k_n sets a characteristic energy scale through $k_n d^2$. Setting $d \to 10\mu m$ and $k_n/d \to 1 \times 10^9$Pa gives dimensional quantities as reported in Figure 9.

The trajectory of each particle is calculated based on Equation 2, where $\Sigma\mathbf{F}$ and $\Sigma\mathbf{\Gamma}$ represent the sums of all particle-particle and particle-fluid forces and torques acting on that particle. The integration is carried out in a step wise, deterministic manner, employing the Velocity-Verlet algorithm to update particle positions and velocities, implemented in LAMMPS[59]. Further justification of the model features and assumptions is given elsewhere[60]. Our simulation approach has previously been validated against experimental data in simple shear flow[42] and under time dependent flows[20,43] and the results compare favourably, both qualitatively and quantitatively.

Per-particle hydrodynamic and contact force dipole contributions are calculated according to

$$\mathbf{\Sigma}_i^H = \sum_{i \neq j} \mathbf{r}_{ij} \otimes \mathbf{F}_{ij}^h, \tag{7a}$$

$$\mathbf{\Sigma}_i^C = \sum_{i \neq j} \mathbf{r}_{ij} \otimes \mathbf{F}_{ij}^c, \tag{7b}$$

respectively[42], where $\mathbf{F}_{ij}^c = \mathbf{F}_{ij}^{c,n} + \mathbf{F}_{ij}^{c,t}$. The stresses that we consider in this work are derived from the total force dipole $\mathbf{\Sigma}_i = \mathbf{\Sigma}_i^H + \mathbf{\Sigma}_i^C$[61] as described below. According to this sign convention, compressive stresses are *positive*.

Geometry and boundary conditions

A model paste described by the above set of interaction forces is extruded through a pseudo-2D square entry extrusion die with geometry and dimensions given in Figure 1. A barrel width of $100d$ and a die width of $20d$ are used to approximate very narrow confinement such as might arise in an industrial extrusion setting, for example the extrusion geometry pertaining to the inner honeycomb walls of a monolithic ceramic catalyst support. While the die width of $20d$ may be realistic for the most narrow of industrially employed extrusion dies, the corresponding barrel width in such an apparatus would generally be considerably larger than $100d$. The present dimensions are chosen, however, to reduce computational expense while retaining relevant features of the geometry such that the resulting velocity and stress profiles may be indicative of those in reality. The geometry is periodic in the z-direction, with a depth of $5d$. This depth was chosen by trading off the need to capture 3D effects with the computational cost of a truly 3D representation of the extruder. Since

z represents the vorticity direction, we do not observe rheological features such as shear banding or boundary effects in z in this case. In related work (Ref[62]) we found negligible difference in our results when extending the z-depth from 5 to 20 particles.

The extruder walls are composed of particles of diameter $0.5d$ at very high area fraction, giving an inherent wall bumpiness that will offer some resistance to flow by allowing the walls to support non-zero loads in the x-direction, Figure 2. Such an approach has been adopted previously to study lubricated suspension flows under confinement[63–65]. The contact model presented previously in this section, comprising hydrodynamic and contact forces, also describes the interaction between paste particles and wall particles, though a separate friction coefficient μ_w is defined independently of μ_p as mentioned above, allowing the frictional behaviour between particles and wall to be different to that for particle-particle contacts. Interactions between neighbouring constituent wall particles are excluded from the numerical integration, effectively freezing those particles in their pre-determined positions. Unlike solid mechanics simulations of smooth walled square entry dies in which static zones are not observed as there is no shear stress to resist motion, our treatment of the die walls allows us to explicitly impose friction such that these shear stresses do arise. As our boundary is composed of small particles, there is an inherent bumpiness that induces some fluctuations and minimal shearing in the bulk paste even when $\mu_w = 0$, leading to some energy dissipation through contact and lubrication forces and hence a non-zero barrel pressure drop. This bumpiness means that the first layer of particles near the wall are located, on average, at $\frac{1}{2}(d_{\text{wall}}+d_{\text{particle}})$, with a small variance due to particles sitting in the shallow interstices. Our boundary further influences the distribution of particles through layering (as we present later in Figure 8, similar to e.g. Ref[66] since the small wall particles approximate a flat surface). We verified that the resulting layering at the wall observed in our system approximates that as would be imposed by a perfectly flat wall. Further, we ensemble average over systems with different wall configurations, and in practice find that measured quantifies including pressure drop and die velocity are extremely insensitive to changes in the arrangement of the fixed wall particles.

A pressure drop along the axial length of the extruder is generated by applying a constant body force F in the $+x$ direction at each timestep to all particles that are inside the dashed box in Figure 1. These particles will consequently move downstream out of the dashed box, where they will exert hydrodynamic and contact forces on neighbouring particles that

eventually percolate the extruder and result in mass flow through the die. The flow rate through the extruder is therefore dependent on the magnitude of the constant force applied in the dashed box. In order to achieve steady flow over large displacements, particles are generated inside the dashed box at each timestep, such that the particle volume fraction (defined as the total volume of particles divided by the total volume) within this region remains at approximately $\phi = 0.5$. Note that there is no imposed volume fraction or particle number in the main body of the extruder: a constant volume fraction and driving force are maintained only within the dashed box. Downstream of this region the system dynamically reaches a local steady state with a driving-force-dependent flow rate, pressure drop and volume fraction. The downstream end of the geometry is open, so particles flowing out of the end of the die are removed from the simulation and subsequently omitted from contact force and stress calculations.

Simulations may be run ad infinitum, meaning time averaged as well as instantaneous flow features can be studied during steady flow. The imposed force magnitudes F implemented in the present work are chosen such that the flow remains close to the hard particle limit, with $F/k_n d \ll 1$ (practically this means particle overlaps, quantified by δ, remain $\ll 0.01d$) and such that overdamping arising due to particle-fluid interactions is sufficiently thorough that particle inertia can be neglected. Conventional wisdom[67–69] suggests that the rheology should consequently be Newtonian in that stresses scale linearly with shear rates, though it remains exquisitely sensitive to particle volume fraction. Significantly larger values of F would lead to $\delta \to \mathcal{O}(d)$, a considerable violation of the approximately hard particle condition. The resultant soft particle rheology[70], reminiscient of emulsions, for example, may be captured by the present model[42] but is beyond the scope of the present study. Moreover, large values of F may further lead to high velocities and localised shear rates for which the Stokes number exceeds 1, meaning the flow might transition from viscous, quasi-Newtonian to inertial[52,71]. We maintain sufficiently small F to avoid these two regimes.

For post-processing, we adopt a simple binning protocol to coarse grain the particle information, obtaining continuous velocity and stress fields. Bins are generated with dimensions $d \times d \times 5d$ on a regular grid in the x–y plane. The properties of each particle are accumulated in a bin if the coordinates of the centre of that particle lie in the bin. Particle velocities $\mathbf{v}_i$ are averaged within each bin, giving a coarse grained velocity vector $\mathbf{V}_k$, which has components $V_{k,x}$, $V_{k,y}$, $V_{k,z}$ where k is the bin index. Per-particle force dipole contributions $\mathbf{\Sigma}_i$

are summed in each bin and divided by the bin volume V_{bin} to obtain the coarse grained stress tensor for each bin $\boldsymbol{\sigma}_k$, which has components $\sigma_{k,xx}$, $\sigma_{k,xy}$ etc. We thus obtain a coarse grained map of the velocity and stress profiles at each timestep which can be used to generate temporally-averaged profiles or to study transient features of the flow. The present study focusses on the steady state flow behaviour of the system; an analysis of the transient behaviour is deferred to future work.

Simulation cases studied

In the present study, we give a general description of the flow features predicted by the above model, followed by an overview of the roles of the model parameters. From the particle-fluid interaction, the available parameters are the magnitude of the Newtonian fluid viscosity η_f and the limiting surface separation constants h_{min} and h_{max}. As discussed above, h_{max} is chosen to be sufficiently large that all immediate neighbours will be considered when calculating the lubrication forces for a particle. It has been confirmed that setting $h_{\text{max}} = 0.1d_{ij}$ does not give significantly different rheological behaviour, though it does significantly increase the computational expense. Furthermore, it has been demonstrated recently[43] that the size of h_{min} is important in determining the response of model pastes to minute deformations[72], but that its influence during large paste deformations and in flows close to steady state is minor. Therefore, the primary fluid parameter available for investigation is the interstitial fluid viscosity η_f.

The parameters present in the particle–particle interaction model are the particle stiffnesses k_n and k_t and the particle–particle and particle–wall friction coefficients μ_p and μ_w respectively. We take $k_t = (2/7)k_n$, following[59]. Each of the other parameters is varied independently, and the influence on flow behaviour is studied. A summary of each of the simulation Cases explored is given in Table I. Values of the particle–wall friction coefficient μ_w are kept low, to represent the very smooth extruder walls found in practice, while further wall resistance derives from the tangential component of the lubrication force acting between paste particles and constituent wall particles.

As argued above, the paste flow regime investigated in this work is a hard-particle, viscous regime. It is therefore anticipated that, provided we remain in this regime, varying the parameters k_n and η_f will have a quantitative, but not qualitative, influence, since the rela-

tive paste viscosity, i.e. the paste viscosity divided by the fluid viscosity η_f, is independent of both when driving forces are scaled appropriately[20,42,73].

PREDICTED EXTRUSION FLOW FEATURES

General description of flow

For each Case, simulations are carried out for pressure drops ΔP, set through the applied driving force F (in units of $k_n d$), spanning two orders of magnitude. Five simulations are carried out for each value of F, each with different precise configurations of wall particles but representing the same large-scale geometry. The following results represent ensemble- and time-averages.

We first present a general picture of the flow features obtained using an initial set of parameters, Case A (Table I). Starting with an empty extruder, the paste flows in at the upstream end as particles are generated and flow is initiated in the dashed box, Figure 1. There is no flow out of the die during this time, so the overall particle number increases steadily. Once the extrusion barrel fills up and a contact network[74,75] establishes between the barrel inlet and the die entry, particles begin to flow into, and through, the die to the outlet, eventually establishing a steady state. The particle number at this point is $\mathcal{O}(10^5)$. It is verified that a steady state has been reached by checking that the mass balance is satisfied such that the total number of particles present inside the extruder is approximately constant with time. Since the particle number is not fixed, the outlet flow minus the inlet flow fluctuates with time around zero.

Extrusion velocity profiles

A contour plot of the time-averaged velocity magnitude ($V = (V_{k,x}^2 + V_{k,y}^2 + V_{k,z}^2)^{1/2}$) profile is given in Figure 3a, for $\Delta P = 5 \times 10^5$Pa, which requires forces $\mathcal{O}(10^{-2})$N. For simplicity of interpretation, the velocity magnitude is scaled according to V/V^{barrel}, where V^{barrel} is the mean centreline (i.e. at axial position $y = 0$) velocity magnitude in the barrel. The associated streamlines are given in Figure 3b, while velocity profiles along lines at $y = 0$,

$x = 150$ and $x = 400$ are given in Figures 3c, d and e, respectively.

Together, the velocity profiles illustrate that there is viscous, uniform flow inside the extruder, that is qualitatively reminiscent of experimental velocity profiles measured using magnetic resonance imaging[76], positron emission particle tracking[77] (though accounting for the fact that they use a cone geometry so have avoided internal shear localisation), and theoretical work by Ref[78]. Specifically, it is observed that there is very little variation along the x-direction in the regions away from the die entry either in the barrel, between the inlet and around 10-20d upstream of the die entry; or in the die, from around 5-10d downstream of the die entry, to the outlet. To clarify this observation, the centreline velocity magnitude $V(y = 0)$ is plotted in Figure 3c. It is observed that the die velocity is approximately 5 times larger than that in the barrel, consistent with the aspect ratio of these regions, satisfying mass conservation.

In both barrel and die, the velocity is highly laminar and nearly independent of y-coordinate, indicating the presence of near-perfect plug flow throughout the extruder, away from the die entry, which we verify in Figures 3d and 3e. The particle–wall friction coefficient μ_w is set to zero in this Case (see Table I), meaning any deviation from ideal plug flow, which would represent perfect wall slip, must be attributable to the inherent bumpiness of the boundary, that derives from its particle-based composition and offers some resistance to flow, supporting loads with non-zero x-components. For the purposes of industrial paste processing, it is desirable to minimize the extent of shearing flow, thus moving the system as close to ideal plug-flow as possible. Perfect slip flow, often facilitated by a liquid slip layer at the boundaries, can lead to smoothly flowing extrudates with minimal surface defects, whereas shear flow close to the paste surface might result in instabilities being generated at the die outlet. Indeed, the present model, with its explicit value for μ_w, may serve as a tool in future studies to investigate the role of wall friction on the formation of shear zones close to extruder boundaries. Note that the streamlines indicate a highly penetrative velocity field, where the flow extends almost completely into the corners of the die entry. Furthermore, even in this region there remains highly viscous flow, with no evidence of recirculating or unstable flow behaviour. It therefore appears that the majority of the deformation, that is, the primary extensional and shearing part of the flow, is concentrated within a very narrow region close to the die entry.

To elucidate the deformation modes acting in this region, we present the velocity gradient

in Figure 4, for shearing $\partial V_x/\partial y$, $\partial V_y/\partial x$ and extensional $\partial V_x/\partial x$, $\partial V_y/\partial y$ flows, noting that the $\partial/\partial z$ terms vanish. In each case, we give the velocity gradient scaled by $\rho d^2/\eta_f$, so that the numerical values act as representative Stokes numbers pertaining to the velocity gradient in the direction of interest: St_{xy}, St_{yx}, St_{xx} and St_{yy}. The velocity gradients reveal considerable shear flow, both along the inner edges of the die, Figure 4a, extending to the outlet (not shown) and, surprisingly, along the vertical inner edges of the die entry, where there is considerable shearing flow in $\partial V_y/\partial x$, Figure 4b. The liquid phase migration paradigm suggests that pressure gradients culminating at the die entry corners lead to liquid migration away from this area. There is a consequent increase in particle concentration leading to jamming or solidification at these regions of the extruder. Instead, the present model suggests that a net flow of particles can be achieved along the inner edge of the die entry, allowing such pressure gradients to dissipate. We note that no significant spatial variations in the solids fraction are identified in the present study.

The flow at the entrance point to the die exhibits significant extension and compression, as indicated by the $\partial V_x/\partial x$ and $\partial V_y/\partial y$ profiles, Figure 4c and 4d respectively. It is observed that the flow entering the die along the vertical extruder walls at the die entry is subject to compression, indicated by the squeezing of the streamlines at this point and the negative $\partial V_y/\partial y$. Simultaneously, the flow entering the die along the extruder axis (near to $y = 0$) undergoes almost pure extension, as shown by the positive $\partial V_x/\partial x$, maintaining the incompressibility of the material. This stretching of the paste entering the die may be indicative of the above mentioned suction effect[31,32,34] that is responsible for drawing liquid out of slower flowing die entry corners into the main extruding flow. These velocity gradients serve to offer a thorough qualitative description of the main deformational flow at the die entry at steady state.

It is noted, particularly in Figure 3, that the flowing regions do not extend fully to the bounding walls at $y = \pm 50$ for $x = 300$, meaning there are small, nearly stagnant, regions in the corners of the die entry. For convenience, the extent of these stagnant regions near the die entrance is quantified by counting the number of coarse-grained cells for which the local velocity $V/V^{\mathrm{barrel}} < 0.25$, and summing all the particles in those cells. The variation of stagnant region size with extrusion velocity is presented in Figure 5. The simulation predicts that static zone size decreases with increasing mass flow rate. A static zone represents a region in which the solid contact network composed of paste particles is nearly stationary,

while in principle the liquid phase may remain mobile by engaging in a porous-media type flow due to the osmotic-like pressure created by the flow in the central region[79] . For paste processing purposes, it is therefore desirable to minimize static region formation. The present results indicate a reduction of static zone size of up to 80% when increasing the die velocity by an order of magnitude, suggesting that liquid phase migration deriving from such static zones may be reduced by operating at increased extrusion velocities. In practice, however, the risk of other instabilities is also introduced when changing the velocity[1], so factors other than the size of the static zone also have to be considered. The evolution of static zone size with increasing die velocity demonstrates that although the bulk $\Delta P \propto V^{\text{die}}$ relationship holds (see later), the paste flow has to be treated as inhomogeneous and subtly rate-dependent in character.

Extrusion stress profiles

We next consider the steady state stress profile in the extruder, focussing on the pressure $P = \frac{1}{3}(\sigma_{xx} + \sigma_{yy} + \sigma_{zz})$, the shear stress σ_{xy}, and the first normal stress difference $N_1 = \sigma_{xx} - \sigma_{yy}$, presented in Figure 6. It is noted that erroneous (i.e. particularly low) stresses are found for $0 < x < 10$ due to the boundary condition being implemented within this region, though the momentum equation remains satisfied when the imposed body forces are taken into account.

a. Pressure profile Consistent with the velocity profile, a rather uniform pressure profile is observed in the main flowing regions of the barrel for $50 < x < 200$, and the die for $350 < x < 450$, away from the die entry. A slight pressure reduction is observed within $10d$ from the barrel walls, where the limited shear flow is sufficient to perturb axially oriented contact chains that propagate from the die-entry corners, though the pressure remains largely uniform across the majority of the barrel width, with σ_{yy} having zero gradient in y, to satisfy momentum conservation. The pressure behaves similarly in the die, with a largely uniform value across the width. We find that the pressure contribution due to the contact forces exceeds that due to hydrodynamics throughout the extruder.

It is found that the variation in x within the barrel ($x < 250$) is small, suggesting that, for the present Case of $\mu_w = 0$, the pressure drop resulting from the inherent wall bumpiness is rather small. By contrast, a significant pressure drop, typically around an

order of magnitude, is then observed at the die entry, in the region $250 < x < 300$. There is a further pressure drop between one and two orders of magnitude, though the absolute value is already considerably reduced following flow through the die entry, along the length of the die. The pressure then drops to zero at the outlet. This axial pressure drop is essentially what drives the net flow of paste through the extruder.

A marked deviation from uniform pressure distribution is observed in the region $250 < x < 300$. An arching effect is observed, whereby regions of high pressure extend from just upstream of the die entry into the stagnant corner zones. The pressure reaches a maximum at these points. This arching pressure appears to be transmitted inhomogeneously through force chains that can be observed as narrow regions of high pressure protruding from near the corners of the square die entry region into the central part of the barrel. Such arching behaviour is reminiscient of simulations of gravity-driven silo discharges[22,23], in which normal and tangential loads supported by frictional walls allow stable bridges to transiently form and collapse. For the nearly-frictionless walls considered in the present simulation, it is expected that the focussing of normal stresses on the square end walls at $x = 300$ will be considerable, since only minimal x-direction loads can be supported by the barrel walls. This is consistent with practice, where the barrel wall is typically lubricated and would bear little load in x. There is a significant pressure drop in the y-direction at the die entry, for $275 < x < 300$. This radial pressure drop between the corners of the die entry and the die entry itself is responsible for the lateral flow of paste observed in this region.

b. Shear stress profile The shear stress contour plot in Figure 6b shows a profile that is comparable to that of the pressure. Notably, there are regions of significantly higher shear stress that correspond to the local arching effects. The shear stress in these regions is, consistent with the pressure, focussed into narrow bands, or chains, that propagate from the central point of the arch to close to the square die corners. The shear stress is approximately symmetrical in magnitude (though opposite in sign) about $y = 0$. Averaging along the barrel, we find linear variation in σ_{xy} between the wall values, but with significant fluctuations arising, particularly close to the die entry.

c. First normal stress difference The first normal stress difference N_1, Figure 6c, quantifies the relative magnitude of the compressive normal forces acting along the downstream (x) and radial (y) axes. The magnitude of N_1 is, significantly, comparable to the pressure. N_1 is positive ($\sigma_{xx} > \sigma_{yy}$) in the bulk region and largely follows the pressure across most of

the extruder, indicating that the paste is compressed more in x than in y, under the influence of the driving upstream force. Notably, however, there is a region of negative N_1 immediately upstream of the die entry. This suggests that the paste is compressed more in the y direction in this region, consistent with the velocity gradient profile (Figure 4) which shows extensional flow (positive $\partial V_x/\partial x$) in this region. Such a normal stress difference would lead to extrudate swell if the stress was relaxed immediately after the die entry without the die land. N_1 is also negative near the barrel walls due to the shearing motion in these regions. In Figure 6d, we rescale the contours to reveal the behaviour of N_1 in the die. We find that up to approximately 50 particle diameters downstream of the die entry, there is considerable inhomogeneity in N_1 across the die width, being negative near the walls and positive in the centre. The inhomogeneity is dissipated as flow proceeds downstream, reaching near homogeneity at the outlet. Such complex N_1 profiles are indicative of a propensity for paste deformation, suggesting that if the die were to be cut short at, say, $x = 325d$, the outgoing flow could be highly unstable. The simulation therefore predicts that extrudate flows might be stabilised by using dies of sufficient length to allow N_1 variations to dissipate.

Though the stress data provide insight into the nature of the flow within the extruder, a more complete description of the origin of the extrusion pressure drop may be obtained by examining the localised rates of energy dissipation. We obtain a coarse grained energy dissipation rate profile S using the coarse grained stress $\boldsymbol{\sigma}$ and strain rate field $\dot{\boldsymbol{\gamma}}$ (obtained from the velocity gradients) according to $S = \boldsymbol{\sigma} : \dot{\boldsymbol{\gamma}}$. We find that the majority of energy dissipation is heavily focussed around the die entry region, with particular emphasis at the corners of the square entry. This result reveals an interesting interplay between the rates of deformation and the stresses near the die entry. Specifically, we note that the maximal rates of dissipation occur at the extreme corners of the square die entry, where the paste is almost stationary as quantified earlier as static regions. Furthermore, it is demonstrated that the regions of highest shear stress, which propagate in narrow bands or chains from near the die corners into the centre of the barrel, do not in fact correspond to regions of significant energy dissipation. Conversely, the low pressure region at the point of die entry, where flow is dominated by extension in x, has a relatively high level of energy dissipation. Together, these results suggest that the most important flow behaviour contributing to the dissipation within the extruder comes from the jamming and nearly arrested flow in the barrel corners, as well as the extensional flow at the die entry. These results provide directly

usable guidelines for extruder design to minimise energy dissipation, and hence pressure drop.

Linking particle properties to extrusion behaviour

The bulk flow behaviour of the paste with respect to the previously identified model parameters is finally assessed by considering the relationship between extrusion flow rate and the extrusion pressure drops and wall stresses. Here, we show the full advantage of our discrete element simulations, by demonstrating how the predicted bulk flow behaviour responds to changes in the particle-scale properties.

The pressure drop is found to vary approximately linearly with extrudate velocity, for the entire range of velocities considered, Figure 9a. Such behaviour may be related to the nature of the lubrication contact model described in the Simulation Model Section, which, assuming sufficiently hard particles and particle Stokes numbers considerably less than unity (which we verified in Figure 4), leads to suspension stresses that scale linearly with shear rates under steady state shear flow[42,67,69]. The dimensional analysis of Boyer et al[69] demonstrates that at vanishing Stokes number there is no intrinsic stress scale in the system and therefore all stresses must scale linearly with shear rates. If we allow particles to come into contact, there may be both contact and hydrodynamic contributions to that stress, both of which scale linearly with the shear rate. In an inertial system such as flowing dry grains, stresses scale with V^2, whereas in the overdamped limit, hydrodynamic and contact stresses scale with velocity V. The viscosity remains dominant even at the walls because in the overdamped limit the particle trajectories are mediated by the interstitial fluid through the lubrication forces even when they have frictional interactions with many neighbouring particles. As a result, we cannot necessarily attribute the flow resistance to hydrodynamics just because it scales viscously. Indeed, as we pointed out earlier, stresses are dominated by contact forces throughout this work. Notably, however, the linear scaling does not, necessarily, imply that the rheology of the material is Newtonian. Specifically, phenomena such as localised volume fraction variations and considerable normal stresses may still arise, leading to a highly complex relationship between the supposed viscosity of the material and the flow circumstances.

As demonstrated by Goyon et al[17], such confined flows can further be subject to strong

spatial cooperativity, or non-local effects[80,81], that in this case relate to how stresses are transmitted from the boundaries through the dense amorphous system. In Figure 8 we present the variations of the stress ratio σ_{xy}/P and volume fraction with $y-$position. We find, interestingly, that the stress ratio at the wall for Cases B and D is quantitatively consistent with values reported by Boyer et al[69] for frictional particles. Moreover, for lower values of μ_w, the stress ratio varies in good agreement with Ref[85]. A consequence of the relatively good agreement of σ_{xy}/P at the wall with experimental values, though, is that the gradient of σ_{xy}/P with respect to y is vastly different in barrel and die, indicating fundamentally different rheology in each region and the lack, therefore, of an intrinsic local flow rule. Further evidence for this comes from the strong spatial organisation at the boundaries, illustrated in Figure 8(c)-(d). Such structure may represent a microstructural source of non-locality and deviation from a bulk local flow rule. Non-locality corresponds to the absence of a local flow rule when comparing flow of a single material in various geometries. As such, the underlying rheology, i.e. the stress-strain rate behaviour, varies considerably between barrel and die[82]. Achieving a deeper understanding of this non-local effect and its implications for continuum descriptions of extrusion flow remains a challenging subject of ongoing work.

It is observed that no apparent bulk yield-stress behaviour is predicted by the present model. This can be explained by the boundary conditions of the simulation, in which the global volume fraction within the extruder is not fixed. Therefore, for any applied force at the barrel inlet, the volume fraction within the extruder evolves over time and eventually adopts a value such that flow may occur. In relation to the Benbow-Bridgwater equation, therefore, we take our bulk material to be representative of a yielded paste, that is, the stresses exceed the yield stress such that the material may flow in the viscous regime. We note that, as a consequence of this assumption, our estimates of energy dissipation rate exclude that portion needed to initially exceed the yield stress.

Other than the oscillating boundary effect illustated in Figure 8 that is consistent with well documented previous works[66,83], the volume fraction throughout the extruder is found to be approximately uniform, with a value that lies marginally below the respective critical volume fraction for jamming[84] for the relevant set of model parameters. It is widely acknowledged that the critical volume fraction for jamming is crucially dependent on the particle-particle friction coefficient[11,36,85]. Simulations in a comparable geometry (Ref 62) indicate that a precompaction process, whereby the paste volume fraction is forced to be

above its critical value for jamming or flow arrest, introduces yield stress behaviour into the material. Similarly, if an air-liquid interface exists, the capillary force could confine the paste to a jammed state leading to yield stress behaviour. The present simulation does not consider such a process, and we emphasize that the simulations probe the flowing state of a fully saturated paste. Thus, the present model may predict yield stresses that arise due to strong confinement effects, but this, and other sources of yield stress behaviour such as particle-particle adhesion[86], are deferred to future investigations.

The variations of extrusion pressure drop ΔP and wall stress τ_w with die velocity are given in Figure 9, for each of the simulation Cases A – F defined previously. We present the total pressure drop, the pressure drop in the barrel, the pressure drop due to paste deformation at the die entry, and the pressure drop in the die. For each pressure drop, results are presented for each of simulation Cases A – F. In addition, a dashed line is included to indicate a gradient of unity. The present results exhibit linear scaling of each pressure drop with respect to extrusion velocity, suggesting rate-independent flowing behaviour, and indicating that the 4- (as opposed to the 6-) parameter Benbow-Bridgwater equation (Equation 1) may be suitable for pastes of repulsive (nearly-) hard spheres in the viscous regime.

Consistent with the previous discussion regarding the independence of rheology on particle stiffness k_n provided the hard-particle limit is adhered to, it is observed in Figure 9 that the results for Cases A and F, corresponding to particle stiffnesses k_n and $2k_n$ respectively, are nearly identical for pressure drop and wall stress. This finding reveals that the extrusion rheology predicted by the present model is independent of particle stiffness, while F remains $\ll k_n d$. Recent experiments using emulsions have illustrated how soft particles might respond in similar flow scenarios[87], suggesting a further future extension of the present model. Comparing Cases A and E, a dramatic increase in extrusion flow rate is observed for reduced suspending fluid viscosity, at fixed ΔP or τ_w. It is noted, however, that this increase in flow rate is approximately two orders of magnitude, for a reduction in η_f of the same proportion. Assuming that local shear rates scale directly with the overall extrusion flow rate and considering the paste flow behaviour in terms of its viscous number $\eta_f \dot{\gamma}/P$[69,88–90], applicable for hard-particle and entirely non-inertial flows, therefore, it is determined that Cases A and E represent comparable flow states, as the viscous number is approximately constant while the local shearing Stokes numbers remain $\ll 1$.

The roles of particle-particle and particle-wall friction are illustrated in Cases A to D.

Total pressure drop predictions (Figure 9a) are in line with expectation: increasing particle-particle friction (compare Cases A, $\mu_p = 1$ and C, $\mu_p = 0.1$) increases total pressure drop and τ_w; increasing particle-wall friction (compare Cases A and B or Cases C and D, $\mu_w = 0$ and $\mu_w = 0.1$ respectively) increases total pressure drop and τ_w. Comparing the relative barrel, die-entry and die pressure drops is, however, more revealing. For flow within the barrel, Figure 9b, the pressure drop is found to be remarkably insensitive to the particle-particle friction, illustrated by comparison between Cases A and C or Cases B and D. Barrel flow is, however, highly sensitive to particle-wall friction, indicating that the entirety of the dissipation within this region derives from particle-wall interactions, regardless of the frictional properties of the particles. Analogous behaviour is observed for the die pressure drop, Figure 9d, though the pressure drop magnitudes are considerably lower than those in the barrel. That the die pressure drop is insensitive to particle-particle friction but highly sensitive to particle-wall friction has important consequences for Benbow-Bridgwater modelling. Specifically, it may be concluded from the present results that the β parameter in Equation 1 is relatively independent of the surface properties of the constituent paste particles, but is highly sensitive to the processing conditions, and linked to the interaction between the paste and the extruder walls that we quantify here using μ_w.

The pressure drop at the die-entry dominates the total pressure drop within the extruder. Comparing Cases A through D reveals that the pressure drop magnitude is sensitive to both the particle-particle μ_p and particle-wall μ_w friction coefficients. From the velocity profile and velocity gradient contour plots in Figures 3 and 4 respectively, it can be deduced that the pressure drop at the die entry derives from both a predominantly elongational paste deformation across $275 < x < 300$, and a lateral (y-direction) flow of material along the bounding wall at $x = 300$. The former may be dominated by details of particle-particle interaction, whereas the latter may be more sensitive to the particle-wall interaction. This dependence implies that the extrusion pressure drop is governed both by the material properties and the processing condition, suggesting a more complex relationship between α and the paste and paste–wall interactions, quantified here as μ_p and μ_w.

Wall stresses are presented in Figure 9(e)-(f) and are found similarly to scale with flow rate. To form an empirical relation between extrusion properties and particle details, a simplistic correlation to fit these wall stress data might be constructed, for example as $\tau_w = (C_1\mu_p + C_2\mu_w + C_3\eta_f)V$ with V the die velocity. Given the approximate collapse

of Cases A and E when written according to a viscous number as discussed above, we expect that a universal value of C_3, perhaps sensitive to ϕ, might be found. For the friction coefficients μ_p and μ_w, however, we find no linear additivity of τ_w contributions. This suggests, as a result, that there is a complex coupling between particle-particle and particle-wall friction, such that the contributions of each may not be built into an empirical model independently. In the absence of such additive rules for incorporating particle-scale physics into empirical relations for extrusion, therefore, our model provides an essential tool which might be exploited in future studies looking comprehensively at, for example, the role of μ_p at fixed μ_w and vice versa.

Our model, therefore, serves as a foundational tool for obtaining bulk extrusion features that arise directly from specified particle-particle and particle-wall interactions. In future, the parameters might be further tuned to investigate specific materials. It is anticipated that the model and the present findings may serve as a framework for establishing links between particle details and paste flow behaviour during extrusion, useful for model development as well as for aiding predictive future paste formulation and process design.

CONCLUDING REMARKS

Using discrete element method simulations of paste extrusion through a square-entry die, we have revealed detailed deformation and stress features, which are difficult to obtain from either experiments or continuum simulations. In particular, combined shear and extensional flow near the die entry is shown through the velocity gradient field; patterns of the normal stress difference are linked to the potential for extrudate swell and flow instabilities at the extruder outlet; energy dissipation is shown to be significant in regions where either stress or extensional deformation rate is high. These insights are useful for practical control or design of paste extrusion processes. Furthermore, our results help to expose the inherently discrete nature of the paste and inhomogeneity of the flow in extruder, drawing on rheological phenomena that originate at the particle-particle interaction level. The model itself may be used directly by industrialists as a tool to inform design and optimisation of extrusion processes, since its implementation is considerably less computationally expensive than alternative multiphase approaches that resolve individual particles and fluid motion. Moreover, the present findings may serve as a basis for future continuum descriptions of

extrusion flow that take full account of the microscale physics that underlie the rheology.

The present model and results may be built upon and utilised in future in a number of ways, in order to strengthen and extend the findings given here. First, the model does not explicitly conserve the mass of the fluid. This means that in regions of volume fraction gradient (which, as we point out above, are very small or negligible in the present case) it is assumed that the fluid may permeate the solid matrix at infinitely high rate. Further work is necessary to test the effect of time-dependent fluid pressure dissipation due to finite permeability during extrusion and may provide a route to linking the present result with those from soil mechanics studies[34]. Another limitation of the model is its inability to capture free surface flows. Specifically, we do not capture the flow behaviour of the paste when it exits the extruder. This is a crucial region of flow, where the engineer typically determines the outcome and success of the extrusion process, i.e. smooth, flowing extrudate or unstable, inhomogeneous, poorly mixed paste. In the present model, we have used the normal stress difference within the die as an indicator of such defects. As it is based on a classical discrete element method algorithm[57], numerous extensions may be made to our model to tailor it to specific pastes or materials of interest. For example, it may be directly extended to account for wide particle size distributions[91], more complex particle-particle interactions such as adhesion[92] or electrostatic repulsion[53], and non-spherical particle shapes[93,94]. Moreover, the geometry might be extended to more complex scenarios, or to truly 3d constrictions, which would provide further evidence for the mechanism of slow and static region formation. In each case, the present model provides a basis for predicting the influence on the overall bulk rheology deriving from these particle details.

Overall, our model and findings have elucidated links between microscale physics and bulk extrusion behaviour, providing a foundation for the development of future continuum models as well as guiding future industrial practice for formulation and design. This can have broad impact on paste processing, and more widely in soft matter rheology across industry.

ACKNOWLEDGEMENTS

This work was funded by the UK Engineering and Physical Sciences Research Council and Johnson Matthey through a CASE studentship award, and benefitted from discussions

with B.M. Guy, M. Hermes and W.C.K. Poon.

NOMENCLATURE

ΔP	Pressure drop
δ	Particle-particle overlap
$\dot{\gamma}$	Shear rate
η_f	Suspending liquid viscosity
$\mathbf{F}^c/\mathbf{\Gamma}^c$	Pairwise contact force/torque
$\mathbf{F}^h/\mathbf{\Gamma}^h$	Pairwise hydrodynamic force/torque
$\mathbf{n}_{ij}$	Particle-particle unit vector
$\mathbf{u}_{ij}$	Particle-particle tangential shear displacement
St	Stokes number
μ_p/μ_w	Particle/wall friction coefficient
ρ	Particle density
Σ	Hydrodynamic/contact stresslet
σ	Stress
A	Extruder outlet cross-sectional area
A_0	Extruder inlet cross-sectional area
d	Particle diameter
h	Particle surface-surface separation
k_n/k_t	Normal/tangential particle stiffness

L Die length

M Die perimeter

m Particle mass

N_1 First normal stress difference $\sigma_{xx} - \sigma_{yy}$

P Pressure

Q Volumetric flow rate

S Rate of energy diddipation

t Time

V Velocity

---

[1] Benbow J, Bridgwater J. *Paste flow and extrusion.* Oxford University Press 1993.

[2] Green A, Stewart G. *Ceramics. A Symposium.* Stoke-on-Trent: British Ceramic Society 1953.

[3] Benbow J, Oxley EW, Bridgwater J. The extrusion mechanics of pastes - the influence of paste formulation on extrusion parameters. *Chemical Engineering Science.* 1987;42:2151–2162.

[4] Horrobin DJ, Nedderman RM. Die entry pressure drops in paste extrusion. *Chemical Engineering Science.* 1998;53:3215–3225.

[5] Draper O, Blackburn S, Dolman G, Smalley K, Griffiths A. Comparison of paste rheology and extrudate strength with respect to binder formulation and forming technique. *Journal of Materials Processing Technology.* 1999;92-93:141–146.

[6] Wilson DI, Rough SL. Exploiting the curious characteristics of dense solid-liquid pastes. *Chemical Engineering Science.* 2006;61:4147–4154.

[7] Martin PJ. *Mechanics of paste flow in radial screen extruders.* University of Cambridge 2002.

[8] Zheng JM, Carlson WB, Reed JS. Flow mechanics on extrusion through a square-entry die. *Journal Of The American Ceramic Society.* 1992;75:3011–3016.

[9] Sollich P, Lequeux F, Hébraud P, Cates ME. Rheology of soft glassy materials. *Physical Review Letters.* 1997;78:2020–2023.

[10] Pham KN, Petekidis G, Vlassopoulos D, Egelhaaf SU, Pusey PN, Poon WCK. Yielding of colloidal glasses. *Europhysics Letters.* 2007;75:624–630.

[11] Guy B, Hermes M, Poon W. Towards a unified description of the rheology of hard-particle suspensions. *Physical Review Letters.* 2015;115.

[12] Brown E, Forman NA, Orellana CS, et al. Generality of shear thickening in dense suspensions.. *Nature materials.* 2010;9:220–224.

[13] Brown E, Jaeger HM. Dynamic jamming point for shear thickening suspensions. *Physical Review Letters.* 2009;103.

[14] Bertrand E, Bibette J, Schmitt V. From shear thickening to shear-induced jamming. *Physical Review E.* 2002;66.

[15] Wagner NJ, Brady JF. Shear thickening in colloidal dispersions. *Physics Today.* 2009;62:27–32.

[16] Lapasin R, Papo A, Rajgelj S. The phenomenological description of the thixotropic behaviour of fresh cement pastes. *Rheologica Acta.* 1983;22:410–416.

[17] Goyon J, Colin A, Ovarlez G, Ajdari A, Bocquet L. Spatial cooperativity in soft glassy flows. *Nature.* 2008;454:84–87.

[18] Seto R, Mari R, Morris JF, Denn MM. Discontinuous shear thickening of frictional hard-sphere suspensions. *Physical review letters.* 2013;111:218301.

[19] Fernandez N, Mani R, Rinaldi D, et al. Microscopic mechanism for shear thickening of non-brownian suspensions. *Physical Review Letters.* 2013;111.

[20] Lin N, Guy BM, Hermes M, et al. Hydrodynamic and contact contributions to continuous shear thickening in colloidal suspensions. *Physical Review Letters.* 2015;115:228304.

[21] Zhou X, Li Z, Fan M, Chen H. Rheology of semi-solid fresh cement pastes and mortars in orifice extrusion. *Cement and Concrete Composites.* 2013;37:304–311.

[22] Holst JMFG, Rotter JM, Ooi JY, Rong GH. Numerical modeling of silo filling. II: discrete element analyses. *Journal of Engineering Mechanics.* 1999;125:104–110.

[23] Wang Y, Ooi JY. A study of granular flow in a conical hopper discharge using discrete and continuum approach. *Procedia Engineering.* 2015;102:765–772.

[24] Khelifi H, Perrot A, Lecompte T, Rangeard D, Ausias G. Prediction of extrusion load and liquid phase filtration during ram extrusion of high solid volume fraction pastes. *Powder Technology.* 2013;249:258–268.

[25] Rough SL, Wilson DI. The production of homogeneous extrudates of microcrystalline cellulose pastes. *International Journal of Pharmaceutics.* 2004;276:185–189.

[26] Andreotti B, Barrat JL, Heussinger C. Shear flow of non-Brownian suspensions close to jamming. *Physical Review Letters.* 2012;109.

[27] Suzuki K, Hayakawa H. Divergence of viscosity in jammed granular materials: a theoretical approach. *Physical Review Letters.* 2015;115.

[28] Yu AB, Bridgwater J, Burbidge AS, Saracevic Z. Liquid maldistribution in particulate paste extrusion. *Powder Technology.* 1999;103:103–109.

[29] Rough SL, Bridgwater J, Wilson DI. Effects of liquid phase migration on extrusion of microcrystalline cellulose pastes. *International Journal of Pharmaceutics.* 2000;204:117–126.

[30] Elhweg B, Burns IW, Chew YMJ, Martin PJ, Russell AB, Wilson DI. Viscous dissipation and apparent wall slip in capillary rheometry of ice cream. *Food and Bioproducts Processing.*

2009;87:266–272.

[31] Mascia S, Patel MJ, Rough SL, Martin PJ, Wilson DI. Liquid phase migration in the extrusion and squeezing of microcrystalline cellulose pastes. *European Journal of Pharmaceutical Sciences.* 2006;29:22–34.

[32] Zhang M, Rough SL, Ward R, Seiler C, Wilson DI. A comparison of ram extrusion by single-holed and multi-holed dies for extrusion-spheronisation of microcrystalline-based pastes. *International Journal of Pharmaceutics.* 2011;416:210–222.

[33] Hongjun L, Leu MC. Liquid phase migration in extrusion of aqueous alumina paste for freeze-form extrusion fabrication. *International Journal of Modern Physics B.* 2009;23:1861–1866.

[34] Patel M, Blackburn S, Wilson D. Modelling of paste flows subject to liquid phase migration. *International Journal for Numerical Methods in Engineering.* 2007;72:1157–1180.

[35] Coussot P. Rheophysics of pastes: a review of microscopic modelling approaches. *Soft Matter.* 2007;3:528.

[36] Sun J, Sundaresan S. A constitutive model with microstructure evolution for flow of rate-independent granular materials. *Journal of Fluid Mechanics.* 2011;682:590–616.

[37] Aydin I, Biglari F, Briscoe B, Lawrence C, Adams M. Physical and numerical modelling of ram extrusion of paste materials: conical die entry case. *Computational Materials Science.* 2000;18:141–155.

[38] Peck MC, Rough SL, Barnes J, Wilson DI. Roller extrusion of biscuit doughs. *Journal of Food Engineering.* 2006;74:431–450.

[39] Roussel N. Steady and transient flow behaviour of fresh cement pastes. *Cement and Concrete Research.* 2005;35:1656–1664.

[40] Engmann J, Mackley M. Semi-solid processing of chocolate and cocoa butter: modelling

rheology and microstructure changes during extrusion. *Food and Bioproducts Processing.* 2006;84:102–108.

[41] Patil PD, Ochoa I, Feng JJ, Hatzikiriakos SG. Viscoelastic flow simulation of polytetrafluoroethylene (PTFE) paste extrusion. *Journal of Non-Newtonian Fluid Mechanics.* 2008;153:25–33.

[42] Ness C, Sun J. Flow regime transitions in dense non-Brownian suspensions: rheology, microstructural characterization, and constitutive modeling.. *Physical Review E.* 2015;91:012201.

[43] Ness C, Sun J. Two-scale evolution during shear reversal in dense suspensions. *Physical Review E.* 2016;93:012604.

[44] Yunker P, Zhang Z, Yodh AG. Observation of the disorder-induced crystal-to-glass transition. *Physical Review Letters.* 2010;104.

[45] Ikeda A, Berthier L, Sollich P. Unified study of glass and jamming rheology in soft particle systems. *Physical Review Letters.* 2012;109.

[46] Brady JF. Stokesian Dynamics. *Annual Review of Fluid Mechanics.* 1988;20:111–157.

[47] Bossis G, Brady JF. Dynamic simulation of sheared suspensions. I. General method. *Journal of Chemical Physics.* 1984;80:5141.

[48] Brady JF, Bossis G. The rheology of concentrated suspensions of spheres in simple shear flow by numerical simulation. *Journal of Fluid Mechanics.* 1985;155:105.

[49] Brady JF. Computer simulation of viscous suspensions. *Chemical Engineering Science.* 2001;56:2921–2926.

[50] Ball RC, Melrose JR. A simulation technique for many spheres in quasi-static motion under frame-invariant pair drag and Brownian forces. *Physica A: Statistical Mechanics and its Applications.* 1997;247:444–472.

[51] Kumar A, Higdon JJL. Origins of the anomalous stress behavior in charged colloidal suspensions under shear. *Physical Review E.* 2010;82.

[52] Trulsson M, Andreotti B, Claudin P. Transition from the viscous to inertial regime in dense suspensions. *Physical Review Letters.* 2012;109.

[53] Mari R, Seto R, Morris JF, Denn MM. Shear thickening, frictionless and frictional rheologies in non-Brownian suspensions. *Journal of Rheology.* 2014;58:32.

[54] Kim S, Karilla SJ. *Microhydrodynamics : Principles and Selected Applications.* Butterworth-Heinemann 1991.

[55] Bossis G, Brady JF. The rheology of Brownian suspensions. *The Journal of Chemical Physics.* 1989;91:1866.

[56] Jamali S, Boromand A, Wagner N, Maia J. Microstructure and rheology of soft to rigid shear-thickening colloidal suspensions. *Journal of Rheology.* 2015;59.

[57] Cundall PA, Strack ODL. A discrete numerical model for granular assemblies. *Géotechnique.* 1979;29:47–65.

[58] Herrmann HJ, Luding S. Modeling granular media on the computer. *Continuum Mechanics and Thermodynamics.* 1998;10:189–231.

[59] Plimpton S. Fast parallel algorithms for short-range molecular dynamics. *Journal of Computational Physics.* 1995;117:1–19.

[60] Ness C, Sun J. Shear thickening regimes of dense non-Brownian suspensions.. *Soft Matter.* 2016;12:914–24.

[61] Gallier S, Lemaire E, Peters F, Lobry L. Rheology of sheared suspensions of rough frictional particles. *Journal of Fluid Mechanics.* 2014;757:514–549.

[62] Unpublished simulation results using a similar contact model but based on a channel flow

geometry (C. Ness and J. Sun).

[63] Nott PR, Brady JF. Pressure-driven flow of suspensions: simulation and theory. *Journal of Fluid Mechanics.* 1994;275:157–199.

[64] Singh A, Nott PR. Normal stresses and microstructure in bounded sheared suspensions via Stokesian Dynamics simulations. *Journal of Fluid Mechanics.* 2000;412:279–301.

[65] Chow E, Skolnick J. Effects of confinement on models of intracellular macromolecular dynamics. *Proc Natl Acad Sci U S A.* 2015;112:14846–14851.

[66] Besseling R, Isa L, Weeks ER, Poon WCK. Quantitative imaging of colloidal flows. *Advances in Colloid and Interface Science.* 2009;146:1–17.

[67] Hinch EJ. The measurement of suspension rheology. *J. Fluid Mech..* 2011;686:1–4.

[68] Cates ME, Wyart M. Granulation and bistability in non-Brownian suspensions. *Rheologica Acta.* 2014;53:755–764.

[69] Boyer F, Guazzelli É, Pouliquen O. Unifying suspension and granular rheology. *Physical Review Letters.* 2011;107.

[70] Seth JR, Mohan L, Locatelli-Champagne C, Cloitre M, Bonnecaze RT. A micromechanical model to predict the flow of soft particle glasses. *Nature Materials.* 2011;10:838–843.

[71] Bagnold R. Experiments on a gravity-free dispersion of large solid spheres in a Newtonian fluid under shear. *Proceedings of the Royal Society A: Mathematical, Physical and Engineering Sciences.* 1954;225:49–63.

[72] Cates ME, Wittmer J, Bouchaud JPP, Claudin P. Jamming, force chains, and fragile matter. *Physical Review Letters.* 1998;81:1841–1844.

[73] Chialvo S, Sun J, Sundaresan S. Bridging the rheology of granular flows in three regimes. *Physical Review E.* 2012;85.

[74] Peters JF, Muthuswamy M, Wibowo J, Tordesillas A. Characterization of force chains in granular material. *Physical Review E.* 2005;72.

[75] Majmudar TS, Behringer RP. Contact force measurements and stress-induced anisotropy in granular materials. *Nature.* 2005;435:1079–1082.

[76] Rabideau BD, Moucheront P, Bertrand F, et al. Internal flow characteristics of a plastic kaolin suspension during extrusion. *Journal of the American Ceramic Society.* 2012;95:494–501.

[77] Wildman RD, Blackburn S, Benton DM, McNeil PA, Parker DJ. Investigation of paste flow using positron emission particle tracking. *Powder Technology.* 1999;103:220–229.

[78] Horrobin DJ. *Theoretical Aspects of Paste Extrusion.* University of Cambridge 1999.

[79] Deboeuf A, Gauthier G, Martin J, Yurkovetsky Y, Morris JF. Particle pressure in a sheared suspension: A bridge from osmosis to granular dilatancy. *Physical Review Letters.* 2009;102.

[80] Kamrin K, Henann D. Modeling the nonlocal behavior of granular flows down inclines. *Soft Matter.* 2014;11:179–185.

[81] Kamrin K, Henann DL. Nonlocal modeling of granular flows down inclines. *Soft Matter.* 2015;11:179–185.

[82] Isa L, Besseling R, Poon WCK. Shear zones and wall slip in the capillary flow of concentrated colloidal suspensions. *Phys. Rev. Lett..* 2007;98:198305.

[83] Louge MY. Computer simulations of rapid granular flows of spheres interacting with a flat, fractional boundary. *Physics of Fluids.* 1994;6:2253–2269.

[84] Liu AJ, Nagel SR. Nonlinear dynamics: Jamming is not just cool any more. *Nature.* 1998;396:21–22.

[85] Da Cruz F, Emam S, Prochnow M, Roux JN, Chevoir F. Rheophysics of dense granular materials: Discrete simulation of plane shear flows. *Physical Review E.* 2005;72.

[86] Luding S. Cohesive, frictional powders: Contact models for tension. *Granular Matter.* 2008;10:235–246.

[87] Hong X, Kohne M, Weeks ER. Jamming is difficult in frictionless 2D hoppers. *arXiv.* 2015;1512.02500:1–7.

[88] Jop P, Forterre Y, Pouliquen O. A constitutive law for dense granular flows.. *Nature.* 2006;441:727–730.

[89] Forterre Y, Pouliquen O. Flows of dense granular media. *Annual Review of Fluid Mechanics.* 2008;40:1–24.

[90] Lemaitre A, Roux JN, Chevoir F. What do dry granular flows tell us about dense non-Brownian suspension rheology?. *Rheologica Acta.* 2009;48:925–942.

[91] Gu Y, Ozel A, Sundaresan S. Rheology of granular materials with size distributions across dense-flow regimes. *Powder Technology.* 2016;295:322–329.

[92] Gu Y, Chialvo S, Sundaresan S. Rheology of cohesive granular materials across multiple dense-flow regimes. *Physical Review E.* 2014;90:1–13.

[93] Estrada N, Taboada A, Radjaï F. Shear strength and force transmission in granular media with rolling resistance. *Physical Review E.* 2008;78:1–11.

[94] Estrada N, Azéma E, Radjai F, Taboada A. Identification of rolling resistance as a shape parameter in sheared granular media. *Physical Review E.* 2011;84:1–5.

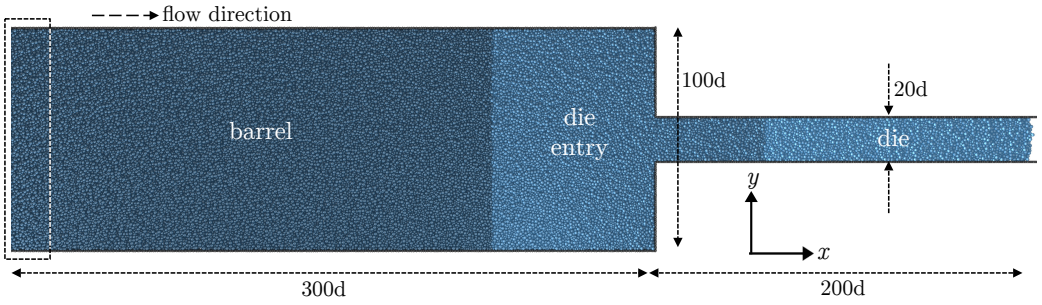

FIG. 1. Schematic of the extrusion geometry showing barrel, die entry and die as represented by different particle shadings, with flow direction from left to right as indicated. Dashed arrows indicate the dimensions in units of particle diameters d; solid arrows indicate the coordinate definition. The geometry is $5d$ deep in the z-direction, with a periodic boundary condition on front and back. The dashed box at the far left illustrates the particle insertion and force application region.

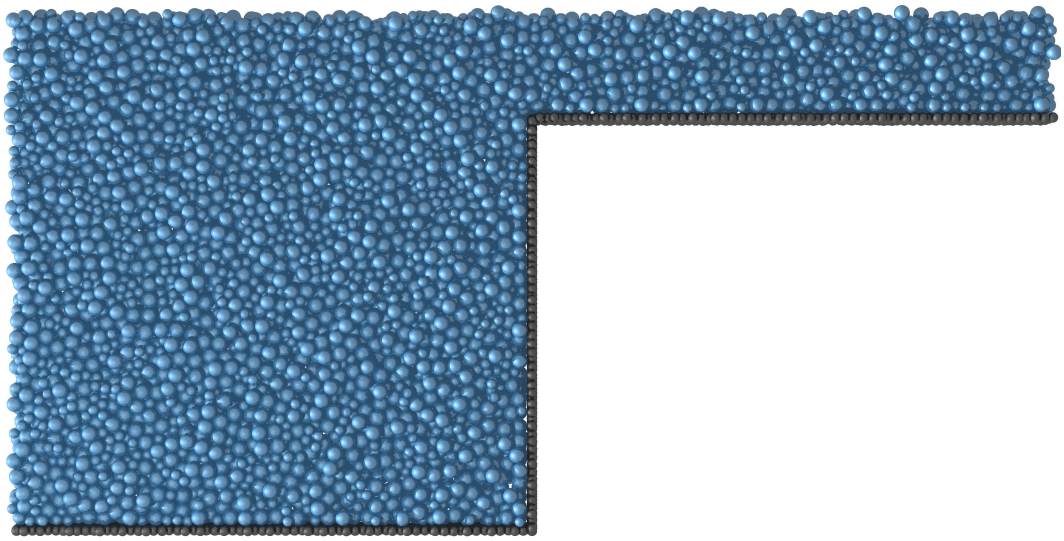

FIG. 2. Close-up image of die entry region, to illustrate the bounding walls composed of nonmoving, smaller particles.

Case	Particle friction μ_p	Wall friction μ_w	Fluid viscosity η_f	Particle stiffness k_n
A	1	0	0.05	10000
B	1	0.1	0.05	10000
C	0.1	0	0.05	10000
D	0.1	0.1	0.05	10000
E	1	0	0.0005	10000
F	1	0	0.05	20000

TABLE I. Summary of particle, fluid and wall properties investigated. η_f and k_n are given in simulation units $\rho d^2/t$ and $\rho d^3/t^2$ respectively, for time unit t, while μ_p and μ_w are dimensionless. In each Case, we set $k_t = (2/7)k_n$.

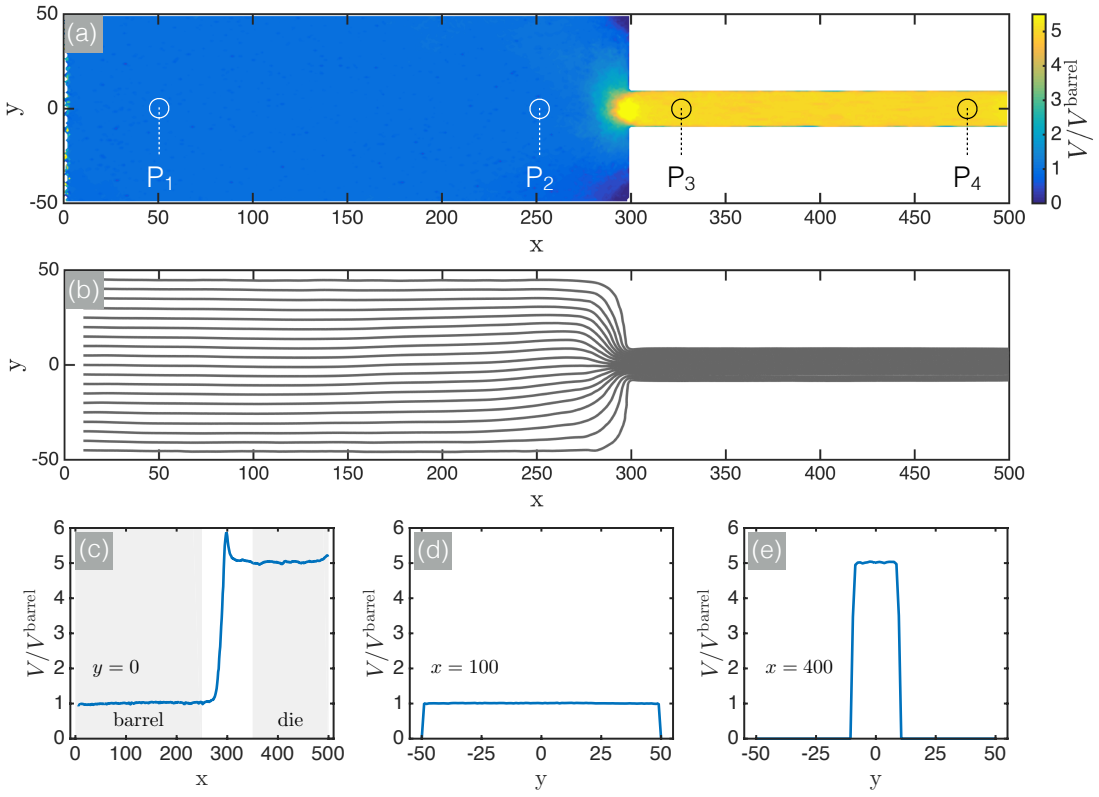

FIG. 3. Velocity profile in the extruder for simulation Case A with $\Delta P = 5 \times 10^5$Pa. (a) Velocity contour plot showing the total velocity magnitude V scaled by the mean centreline downstream velocity in the barrel V^{barrel}. Annotations show the locations of four pressure transducers; (b) Streamlines associated with (a); Velocity profiles along (c) $y = 0$, showing the locations of the barrel and die; (d) $x = 150$; (e) $x = 400$.

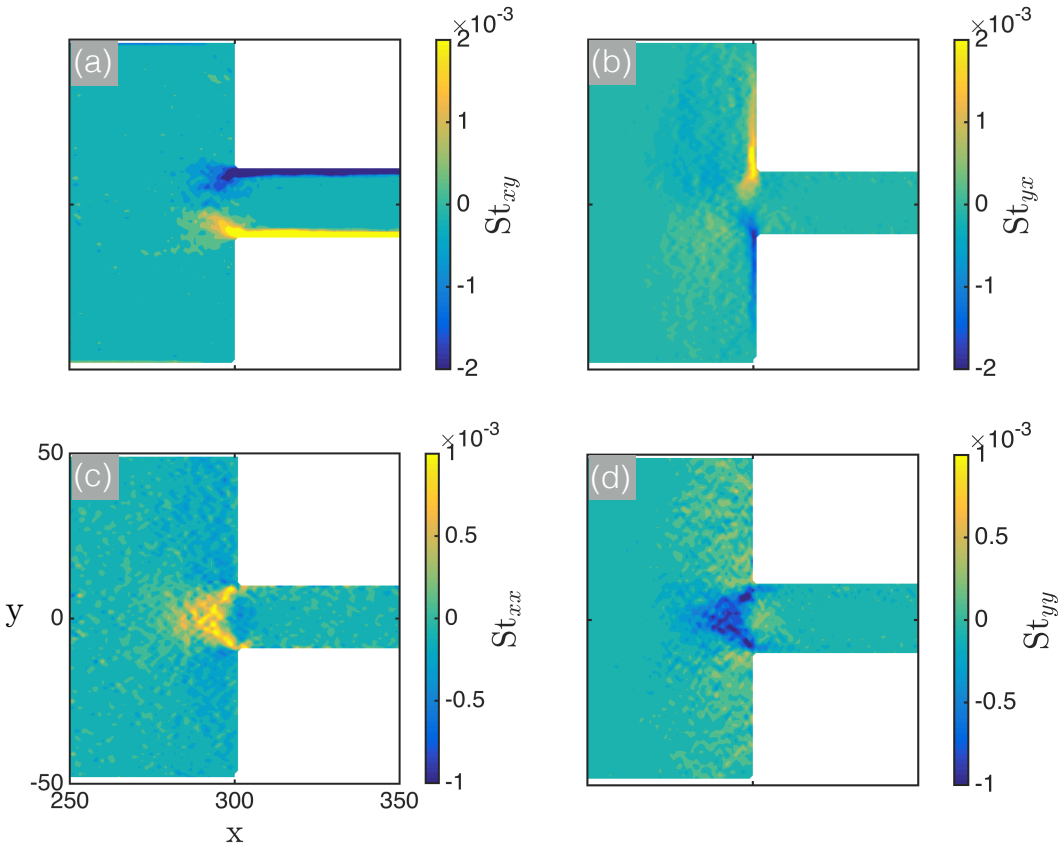

FIG. 4. Velocity gradients at the die entry for simulation Case A with $\Delta P = 5 \times 10^5$Pa, showing shear gradients (a) dV_x/dy; (b) dV_y/dx and extensional gradients (c) dV_x/dx; (d) dV_y/dy. Velocity gradients are scaled with $\rho d^2/\eta_f$ such that the color scale represents Stokes numbers with respect to each flow gradient: (a) St_{xy}; (b) St_{yx}; (c) St_{xx} and (d) St_{yy}. Stokes numbers remain $\ll 1$ in all regions.

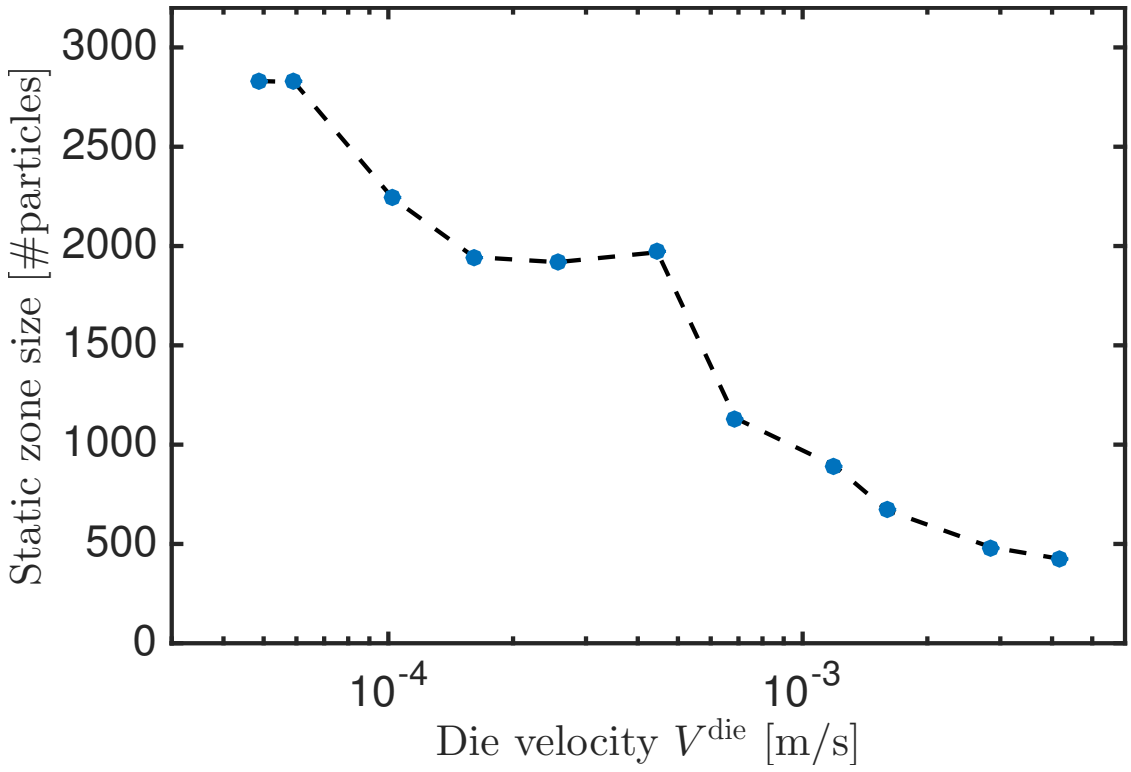

FIG. 5. Time-averaged static zone size for simulation Case A, counting all particles within the static zones, as a function of the die velocity V^{die}.

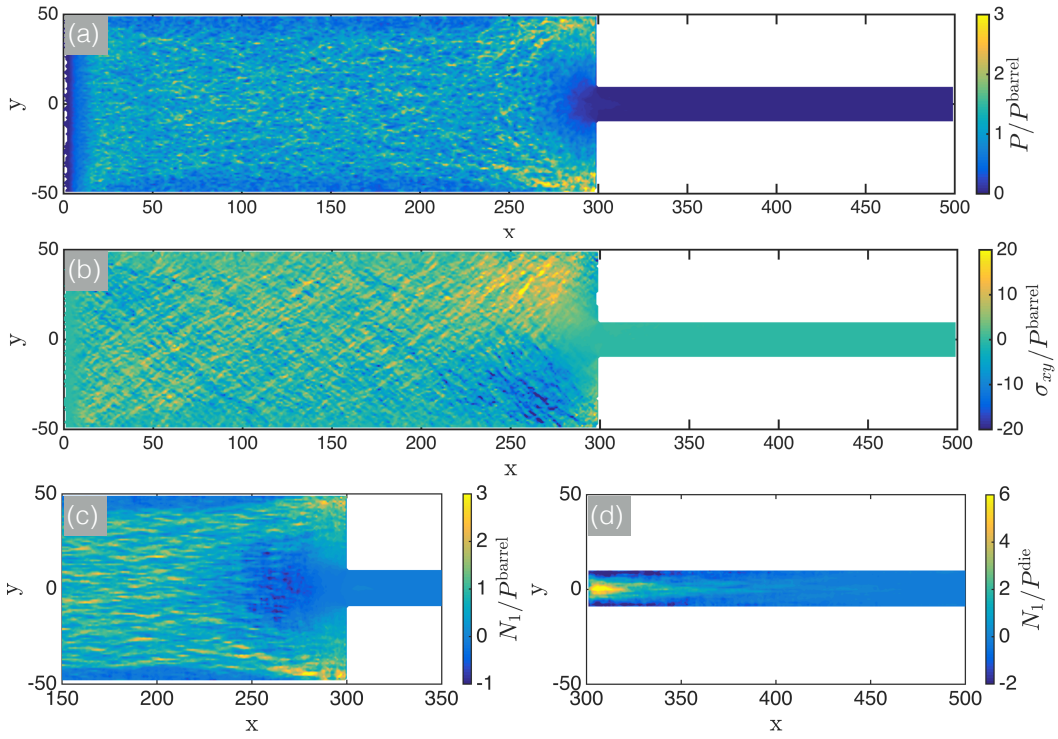

FIG. 6. Internal stress profiles for simulation Case A with $\Delta P = 5 \times 10^5$Pa. (a) Pressure P, scaled by the mean pressure at the upstream end ($25 < x < 50$) of the barrel, P^{barrel}; (b) Shear stress σ_{xy}, scaled by P^{barrel}; (c) First normal stress difference $N_1 = \sigma_{xx} - \sigma_{yy}$, scaled by P^{barrel}; (d) First normal stress difference N_1, scaled by the mean pressure at the upstream end ($300 < x < 325$) of the die, P^{die}.

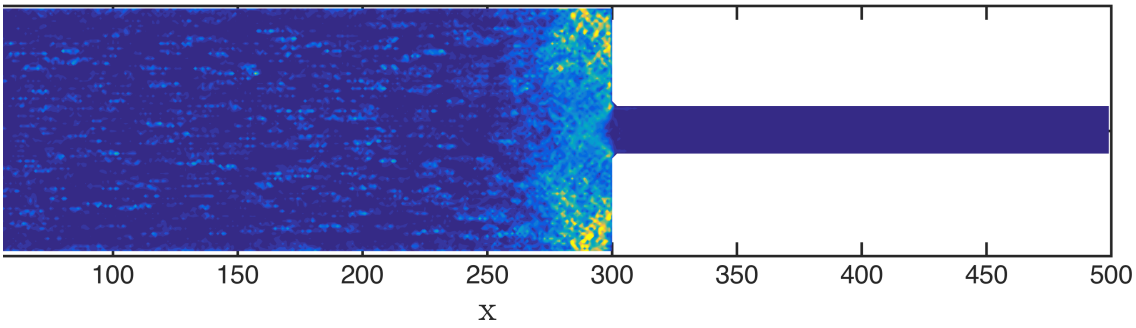

FIG. 7. Rate of energy dissipation per unit volume for simulation Case A, calculated as $S = \boldsymbol{\sigma} : \dot{\boldsymbol{\gamma}}$, where S has units of $\rho d^2/t^3$.

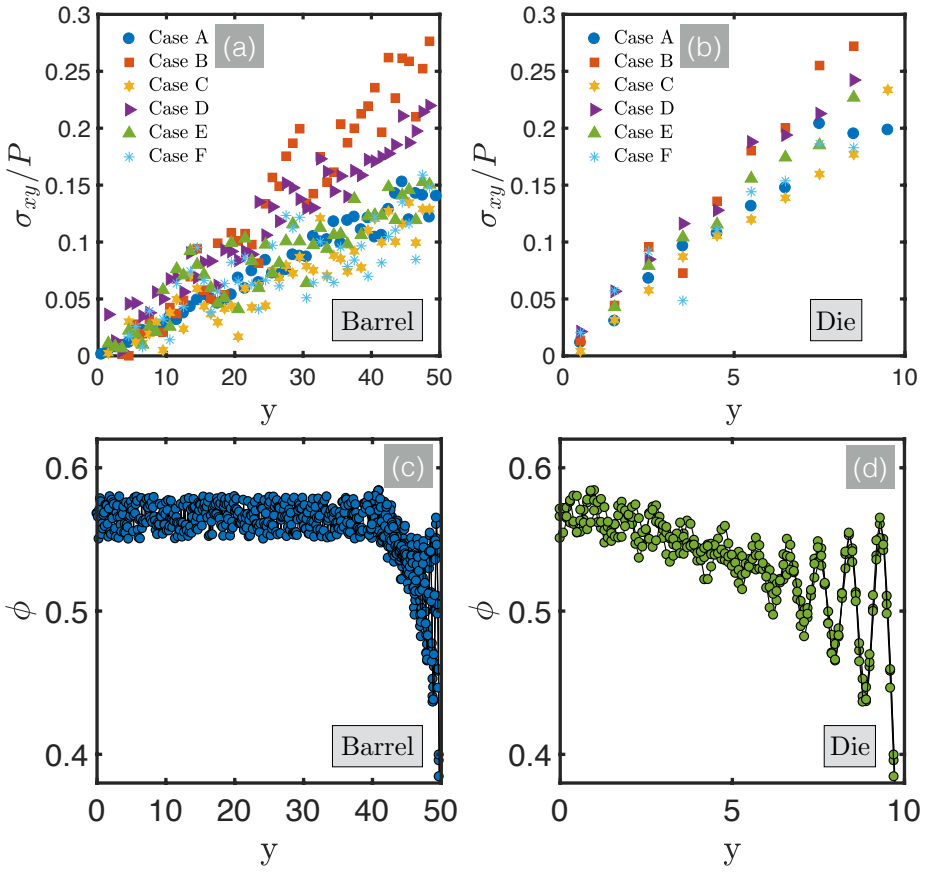

FIG. 8. Stress ratio and volume fraction in the barrel and die. (a) Stress ratio σ_{xy}/P profile in the barrel for Cases A-F; (b) Stress ratio σ_{xy}/P profile in the die for Cases A-F; (c) Volume fraction profile across the barrel for Case A; (d) Volume fraction profile across the die for Case A. The volume fraction profiles for other Cases are analogous to that for A, though with the centreline ϕ being dependent on μ_p.

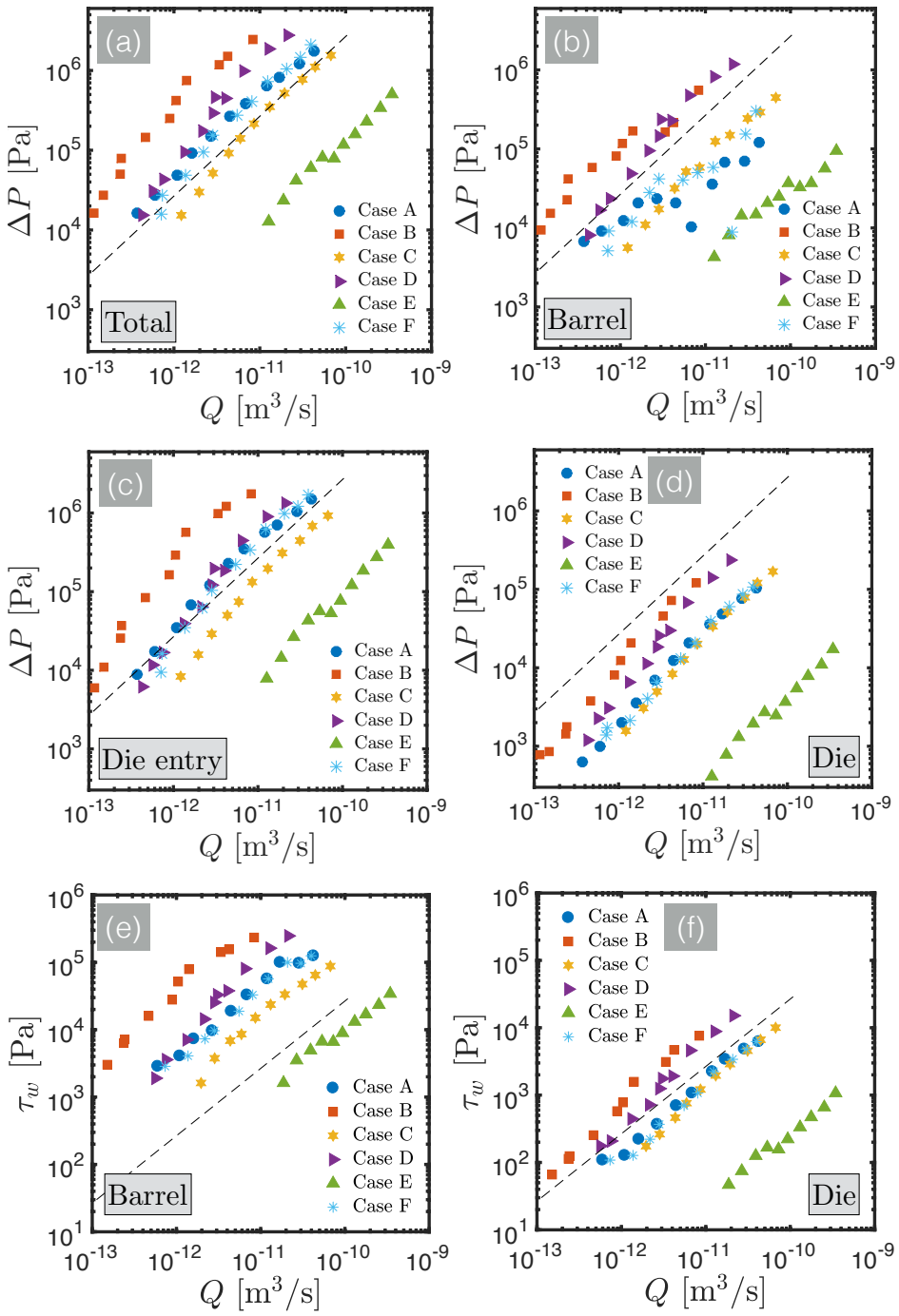

FIG. 9. Pressure drops are wall stresses versus die velocity for simulation Cases A - F, as described in Table I, with the pressures measured at the locations highlighted in Figure 3. (a) Total pressure drop across extruder ($P_1 - P_4$); (b) Barrel pressure drop ($P_1 - P_2$); (c) Die-entry pressure drop ($P_2 - P_3$); (d) Die pressure drop ($P_3 - P_4$). Dashed black line in each figure indicates a gradient of unity; (e) Wall stresses in barrel; (f) Wall stress in die.